

# Small-angle Neutron Scattering (SANS) Characterization of Clay- and Carbonate-rich Shale at Elevated Pressures

Chelsea W. Neil,\* Rex P. Hjelm, Marilyn E. Hawley, Erik B. Watkins, Cody Cockreham, Di Wu, Yimin Mao, Timothy B. Fischer, M. Rebecca Stokes, and Hongwu Xu

Cite This: *Energy Fuels* 2020, 34, 8178–8185

Read Online

ACCESS |

Metrics & More

Article Recommendations

Supporting Information

**ABSTRACT:** Unconventional oil and gas from shale formations have emerged as some of the fastest growing energy resources in the United States, providing both cleaner energy to consumers and reducing the nation's reliance on energy imports. To properly harness these important natural resources, the nanopore structure of associated shales must be fully understood, particularly under hydraulic fracturing conditions, where they are exposed to both overburden compressive and hydrostatic fluid pressures. The current study uses small-angle neutron scattering (SANS) to characterize pore structure, including porosity, pore accessibility, and pore size distribution, in the 1–100 nm regime at elevated pressures for mineralogically distinct clay- and carbonate-rich shales from the Permian Basin. Unlike typical porosity measurement techniques, SANS is uniquely capable of characterizing both open and closed porosity, allowing measurement of how pore accessibility changes with pressure and determination of the size range of accessible versus inaccessible pores. The porosity of the clay-rich shale was 7.7%, compared to 0.51% for the carbonate-rich shale. However, only 2.6% of the nanopores in the carbonate-rich shale were inaccessible to water at 8 kPSI (55.1 MPa) compared to 7.8% for the clay-rich shale. Further analyses indicated that the closed pores fall within distinct size ranges, likely corresponding with the chemical nature of the pore host material. These results provide valuable insight into the effects of shale petrophysical properties on hydrocarbon extraction from unconventional reservoirs.

## 1. INTRODUCTION

As conventional hydrocarbon resources dwindle, new technological developments have allowed for increased production of oil and gas from shale and other tight rock formations. Shale gas production in particular has increased from 1% of the total U.S. gas supply in 2000 to 64% in 2018 and is forecast to account for more than three-quarters of natural gas production by 2050.<sup>1</sup> By 2040, shale gas is expected to provide 40% of the nation's energy,<sup>2</sup> making it one of the fastest growing energy resources. Shale oil production, meanwhile, increased from less than 0.5 million barrels of oil per day in 2008 to over 4 million barrels of oil per day in 2015 and provides about half of U.S. produced crude oil.<sup>3</sup> However, the U.S. still imports the other half of its utilized oil to meet total crude oil needs, and shale oil production is predicted to decline in the 2020s barring the discovery of new resources or improved recovery technology.<sup>1</sup>

Hydrocarbons trapped in shale are accessed through hydraulic fracturing. During hydraulic fracturing, fluid is pumped into a well at a high rate, increasing the pressure enough to fracture the rock formation.<sup>4</sup> These fluids can be water-, oil-, acid-, foam-based, etc. Chemicals are often added to water-based fluids to increase viscosity and prevent fluid-loss, and a proppant such as fine-grained sand is added to prop fractures open. Rock fracturing pressure can be determined using both theoretical and empirical methods.<sup>5</sup> For example, acoustic emission tests can be used to measure the progression of hydraulic fracturing both in the laboratory<sup>6</sup> and in the field,<sup>7</sup> while equations utilizing the *in situ* stress and tensile strength

of the geomaterial can be used to calculate a hydraulic fracturing pressure.<sup>8</sup>

To efficiently harness this valuable energy resource, it is vital to understand the shale matrix characteristics and the extent to which hydraulic fracturing can access hydrocarbons trapped in nanosized pores while under pressure and stress conditions similar to those in the field. Typical porosity measurement techniques, such as gas sorption and mercury porosimetry, which can measure only open pores, are limited to probing pore spaces larger than the intruding molecule.<sup>9</sup> However, in the case of shale undergoing hydraulic fracturing, it is important to quantify both closed and open pores to determine how changing pressure conditions can impact the accessibility of pores where oil and gas are trapped. To achieve these measurements, a number of recent studies have employed small-angle neutron scattering (SANS) to examine shale porosity *in situ* and to characterize porosity changes induced by increasing pressure.<sup>9–13</sup> SANS is uniquely capable of probing both the open and closed porosity of shale.<sup>9,14</sup> Furthermore, due to the high penetration power of neutrons, SANS can be readily combined with robust sample environmental systems, such as a pressure cell,<sup>15</sup> to probe the

Received: March 30, 2020

Revised: May 15, 2020

Published: June 12, 2020

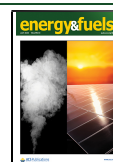


**Table 1. Quantitative XRD Characterization of Carbonate-rich and Clay-rich Shales Showing Their Mineral Compositions (wt %)<sup>a</sup>**

sample ID	calcite (4.69)	dolomite/ankerite (5.44/5.17)	total carbonate	quartz (4.18)	K-feldspar (3.71)	plagioclase (3.97)	pyrite (3.81)	fluorapatite (4.34)	organic matter (~3.6–4.1)	sum non-clay	chlorite (4.58)	illite/smectite (3.78/3.46)	sum clay	total
A	1	1	2	52	4	4	2	3	5	71	0	29	29	100
B	85	6	91	4	0	3	0	1	0	99	0	1	1	100

<sup>a</sup>Values in parentheses are scattering length densities ( $\times 10^{-10} \text{ cm}^{-2}$ ) calculated from [ncnr.nist.gov/resources/activation/](http://ncnr.nist.gov/resources/activation/) or are taken from the literature.<sup>39</sup>

structures and properties of a sample at relevant pressure/temperature conditions.<sup>16,17</sup>

SANS has been used extensively for shale pore structure characterization under ambient conditions.<sup>18–21</sup> However, more comprehensive studies are needed to systematically characterize shale in a way that can be applied to a variety of shale formations at field conditions. For example, there are limited studies available that relate SANS porosity measurements to shale mineralogy, and no studies have achieved these measurements under simulated overburden stress. This study therefore aims to quantify and characterize porosity, structure, and accessibility to water (which serves as a frack fluid) in clay-rich and carbonate-rich shale samples using *in situ* SANS at hydrostatic and overburden pressures up to 8 kPSI (55.1 MPa). Pore accessibility was probed and the scattering profiles were fit to gain insight into how the pore size is related to accessibility. These new findings not only add to our fundamental understanding of shale nanopore characteristics but can also be used by industry to ensure more effective hydraulic fracturing.

## 2. EXPERIMENTAL METHODS

Note: The identification of any commercial product or trade name does not imply endorsement or recommendation by the National Institute of Standards and Technology.

**2.1. Sample Characterization.** **2.1.1. Quantitative Phase Analysis by X-ray Diffraction (XRD).** Shale samples were obtained by Chevron from the Permian Basin. Two samples were chosen for detailed SANS analysis due to their different mineral compositions. One sample, A, was clay rich, and the other, B, was carbonate rich. The mineral compositions of these two samples were quantified using X-ray diffraction (XRD). XRD data were collected on a Siemens D-5000 diffractometer equipped with a 40-position sample holder, theta–theta goniometer, and a Kevex Peltier cooled silicon solid-state detector. Cu K $\alpha$  radiation was used, and the applied voltage and current were 50 kV and 40 mA, respectively. In order to achieve quantitative analysis, samples were spiked with 10 wt % zincite as a reference standard prior to milling with a McCrone mill. Samples were prepared following the methods outlined in Środoń et al.<sup>22</sup> and Omotoso et al.<sup>23</sup> with the intent of making randomly oriented, isotropically scattering samples. Chevron's proprietary QUANTA software was used to quantify mineral percentages in these samples. QUANTA is a modification of the matrix-flushing technique used by Chung.<sup>24</sup> Total organic carbon (TOC) values were obtained commercially at Weatherford Laboratories (Houston, TX) using LECO TOC and RockEval II pyrolysis. Although the fraction of carbon in organic matter (OM) related to TOC can vary by a quotient between 0.79 to 0.89, which increases with thermal maturity,<sup>25</sup> in the absence of this specific data, the average carbon concentration reported in Jarvie<sup>26</sup> of 0.833 was chosen. OM values were calculated by dividing by this factor and incorporating it into the XRD quantification. The mineralogy and OM were then renormalized to a sum of 100%.

**2.1.2. Differential Scanning Calorimetry (DSC)/Thermogravimetry (TG).** To determine the water and carbon contents of the shale samples and to examine their thermal behavior, TG and DSC

measurements were conducted using a Netzsch simultaneous thermal analyzer (STA) 449 system. About 15 mg of clay-rich, A, or carbonate-rich, B, shale sample powders were packed in a standardized Pt crucible. The loaded crucible was then placed into the calorimeter and heated to 1273 K at a rate of 10 °C/min under an Ar atmosphere. For baseline correction, an earlier scan using the empty Pt crucible was run under the same conditions. Temperature was calibrated against the melting points of several metal standards (e.g., In and Al), and sensitivity calibration was done using the heat capacities of sapphire. This technique has been used to study other volatile-bearing samples.<sup>27–29</sup>

**2.1.3. X-ray Computed Tomography (XCT).** X-ray computed tomography was used for image-based characterization. During XCT, an X-ray beam is passed through the sample, where it is attenuated by different minerals in the sample. Transmitted X-ray intensity is influenced by the density and composition of the mineral grain or substance along the X-ray path through the sample. In reconstructed 3D tomographic images, low electron density materials appear darker due to having low X-ray attenuation, while higher density materials are bright.<sup>30</sup> This technique is especially valuable for shale characterization due to its heterogeneity. A series of XCT scans were performed on two clay- (A) and carbonate-rich (B) shale sample cores, 1 or 1.5 in. in diameter (2.54 or 3.81 cm) and 1–2 in. in length (2.54 to 5.08 cm).

**2.2. Small-Angle Neutron Scattering (SANS) Measurements.** SANS uses a collimated neutron beam to probe the nanoscale structure of a sample over length scales from approximately 1 nm to roughly 100 nm. This technique measures elastic scattering due to neutron interaction with nuclei in a sample. As a result, unlike X-ray scattering, SANS is sensitive to light element contrast and isotopic composition of a sample.<sup>31,32</sup> This, with its aforementioned penetrating power, makes SANS ideal for studying bulk geomaterials in robust sample environments. Each element or its isotopes has a characteristic scattering length proportional to the amplitude of the scattered wave. The scattering length density (SLD,  $\rho$ ) of a material can be calculated from the sum of the nuclear scattering lengths,  $b_i$  (cm), of the atoms in a given volume,  $V$  ( $\text{cm}^{-3}$ ), as

$$\rho = \frac{\sum_i b_i}{V} \text{ (cm}^{-2}\text{)} \quad (1)$$

using its isotopic and elemental composition and density. Scattering intensity is proportional to the average spatial fluctuations in contrast squared,  $\overline{\Delta\rho^2}$ , over the volume sampled by the neutron beam. SANS analysis of pore accessibility and structure approximates the shale as consisting of two phases: pores, which are initially empty, and the rock matrix, made up of the shale components listed in Table 1. For this model we define a contrast term,  $\Delta\rho = \rho_p - \rho_m$ , where  $\rho_p$  refers to the SLD of the pore and  $\rho_m$  refers to the SLD of the shale matrix.

An important application of this model is the technique of contrast matching. Equation 1 was used to determine the average  $\rho_m$  from the mineral compositions shown in Table 1 to be  $4.67 \times 10^{-10} \text{ cm}^{-2}$  for the carbonate-rich (B) and  $3.81 \times 10^{-10} \text{ cm}^{-2}$  for the clay-rich (A) shale samples. These values are significantly different from an empty pore, which has an SLD of approximately zero. To achieve contrast matching, samples are imbibed with water that is a mixture of D<sub>2</sub>O and H<sub>2</sub>O. D<sub>2</sub>O has an SLD of  $6.36 \times 10^{-10} \text{ cm}^{-2}$ , and H<sub>2</sub>O has an SLD  $-0.56 \times 10^{-10} \text{ cm}^{-2}$ . These two forms of water can thus be used to produce mixtures of D<sub>2</sub>O/H<sub>2</sub>O with an SLD matching that of  $\rho_m$ .

These D<sub>2</sub>O/H<sub>2</sub>O solutions are 76% D<sub>2</sub>O for Shale B and 64% D<sub>2</sub>O for Shale A. When these contrast-matching mixtures are introduced into the pores of the respective samples, their scattering contrast,  $\Delta\rho$ , becomes negligible, leaving scattering from pores which are inaccessible to the contrast matching solution as the dominant source of scattering intensity, thus providing a means to discriminate between open and closed pores. Pressure is required to introduce the fluid into some of these open pores; as pressure is increased and more pores become accessible, scattering intensity continues to drop.

A general term for SANS intensity,  $I(Q)$ , assuming that only pores not filled with contrast-matching fluid contribute to the scatter, is given as

$$I(Q) = N_T \int P(R)I(Q, R) dR \quad (2)$$

Here,  $Q = \frac{4\pi}{\lambda} \sin \theta$  is the scattering wavenumber ( $\text{\AA}^{-1}$ ), where  $\lambda$  is the incident neutron wavelength and  $2\theta$  is the scattering angle;  $N_T$  is the number density of voids ( $\text{cm}^{-3}$ );  $P(R)$  is the probability density function (PDF) of voids with size and shape given by the set of dimensional parameters,  $R$ ; and  $I(Q, R)$  is the scattering intensity from a single void with these parameters. The intensity from a single void is

$$I(Q, R) = \Delta\rho^2 [V(R)]^2 F(Q, R) \quad (3)$$

where  $V$  is the void volume and  $F$  is the form factor, which is the scatter from a single void normalized for its volume and contrast. Our challenge is to invert the data, as expressed in eq 2, to determine the PDF for the unfilled voids with pressure.

In eq 2, we ignore the intervold connectivity and large scale surface structure that contribute to the scatter at low  $Q$ , as this contribution is factored out in the analysis. This low  $Q$  scattering from shale takes on a power law:

$$I(Q) \sim Q^{-D} \quad (4)$$

For values of  $D$  between 3 and 4, scattering can be interpreted as resulting from surface geometry or from pore size polydispersity.<sup>33</sup> Values of  $D$  less than 3 indicate particle and particle aggregate geometry, with noninteger values interpreted as being characteristic of fractal-like hierarchical structure.<sup>34</sup>

The PDF was calculated using the size distribution macro in the Irena Tool Suite. This fitting tool factors out the low  $Q$  power law scattering as not being relevant to the smaller void PDF. The pore size distribution function is then computed from the residual. The Irena tool computes size distribution for spherical pores as an approximation of the distribution function for oriented ellipsoids viewed along the rotation axis for the isotropic SANS in sample B and along a slightly tilted axis for sample A. Thus, the SANS, which samples the Fourier space along a plane through the origin of Fourier space perpendicular to the viewing axis, is not quite the same for an ordered ellipse as for a sphere. However, we do not consider this distinction important to our measurements, as our goal was to quantify the pressure induced changes in pore contribution to the scattering intensity and not the pore morphology.

SANS experiments were conducted on the NGB 30m SANS instrument<sup>35</sup> at the NIST (National Institute of Standards and Technology) Center for Neutron Research (NCNR). Due to the limited number of samples run, it is difficult to assess how representative these samples are. However, replicate measurements of Shales A and B were conducted dry at ambient pressure (Figure S1 in the SI) and showed similar trends in the average pore size and distribution. Replicate measurements at higher pressures were not possible due to long required measurement time and limited neutron beam availability. Incident neutron  $\lambda$  was 5  $\text{\AA}$  with a resolution,  $\Delta\lambda/\lambda$ , of 13%. This wavelength and a 300  $\mu\text{m}$  sample thickness were chosen as to reduce the likelihood of multiple scattering. The samples were prepared with the intention of being cut parallel to the bedding plane; however, in the case of the clay-rich Shale A, the sample was slightly askew, leading to the anisotropy described in Section 3.2. The sample-to-detector distances were set at 3 and 12 m to give a  $Q$  measurement domain of 0.003 to 0.2  $\text{\AA}^{-1}$ . The area probed by SANS measurement,

defined by the acceptance aperture of the flow-through pressure cell, was 0.25" (6.4 mm).<sup>14</sup> NIST's data reduction package was used to reduce SANS data to differential cross section per steradian per unit volume ( $\text{cm}^{-1}$ ).<sup>36</sup>

Measurement of shale samples at elevated pressures was accomplished using a flow-through pressure cell, whose development and method of use were previously described by Hjelm et al.<sup>15</sup> This device simultaneously applies uniaxial compressive (overburden) stress,  $\sigma_{ax}$  and hydrostatic fluid (pore) pressure,  $p$ , with effective stress,  $\sigma_e = \sigma_{ax} - p$ , up to 60 MPa, using two ISCO series 100HLfd syringe pumps. A schematic of this cell can be found in Figure S2. Pressures were controlled and data-logged using the program Disco.<sup>15</sup> The compressive and hydrostatic pressures were set with the later 200 PSI (1.4 MPa) higher, giving approximately a null total stress on the sample (e.g., overburden pressure was set to 8.2 kPSI when the pore pressure was 8 kPSI). This procedure thus prevented unintended sample swelling and pore structure alteration.

Although the method of measuring shale porosity with SANS has been previously established, the experiments and results in this publication are first-of-their-kind, in that we are able to measure the simultaneous effects of both pressure and overburden stress, representing the real field conditions of shale at various depths. For each sample, SANS measurements were taken of the dry shale sample and sample which was wetted at ambient pressure. The compressive and hydrostatic pressures were then increased incrementally to 8 kPSI (55.1 MPa), with measurements taken at least every 1 to 2 kPSI (6.9 to 13.8 kPa). Measurements were conducted at ambient temperatures.

Due to its extremely low permeability, we conducted an additional test on the clay-rich shale to ensure that it is close to equilibrium saturation for these measurements, particularly at ambient pressure where saturation is expected to occur most slowly. Results can be found in Figure S3. There was no difference in the empty pore scattering intensity or pore size distribution with soaking time after the initial 5 min, indicating that the sample saturated quickly.

Pore size distributions and accessibility were determined using the Irena "Size Distribution" macro with the maximum entropy method.<sup>37</sup> Porosity was calculated using the invariant method.<sup>38</sup>

### 3. RESULTS AND DISCUSSION

**3.1. Sample Characterization.** Table 1 lists results from the XRD measurement of Shale A and B samples. The clay-rich sample, A, primarily consisted of quartz (52 wt %) and illite-smectite (29 wt %, >95% illite). The carbonate-rich sample, B, consisted of 85 wt % calcite and only 1 wt % clay minerals. Further characterization using TGA/DSC supported this observation, with pyrolysis of kerogen and clay dehydroxylation observed only in Shale A, while XCT imaging revealed the presence of a very dense material, likely to be pyrite as indicated by XRD, solely in the clay-rich, Shale A sample. These observations indicate positive correlations of TOC with the clay and pyrite contents. TGA/DSC graphs and XCT images can be found in Figure S4.

**3.2. SANS Profiles.** SANS measurements revealed that scattering was isotropic for Shale B, as shown by an azimuthal trace of the 2D data at constant  $Q$ , where the scattering intensity is constant over the entire range (Figure S5). For Shale A, the scatter was anisotropic, as shown by a nonuniform azimuthal trace with the highest intensities at around 100° and 250°. This result is consistent with previous reports of shale where the anisotropy relative to the bedding plane is interpreted as due to predominately ellipsoidal voids with the large axis parallel to the bedding plane.<sup>40,41</sup> According to this interpretation, the anisotropy observed in Shale A is the result of the shale section not being exactly parallel to the bedding plane.

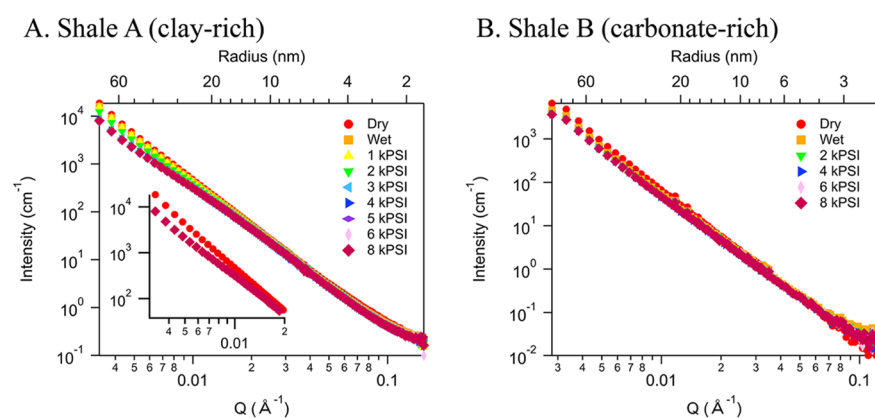


**Figure 1.** SANS profiles for (A) clay-rich shale and (B) carbonate-rich shale exposed to a contrast matching  $D_2O/H_2O$  solution. The inset in Figure 1A shows the bend formation occurring at  $Q < 0.02 \text{ \AA}^{-1}$  for Shale A at high pressures.

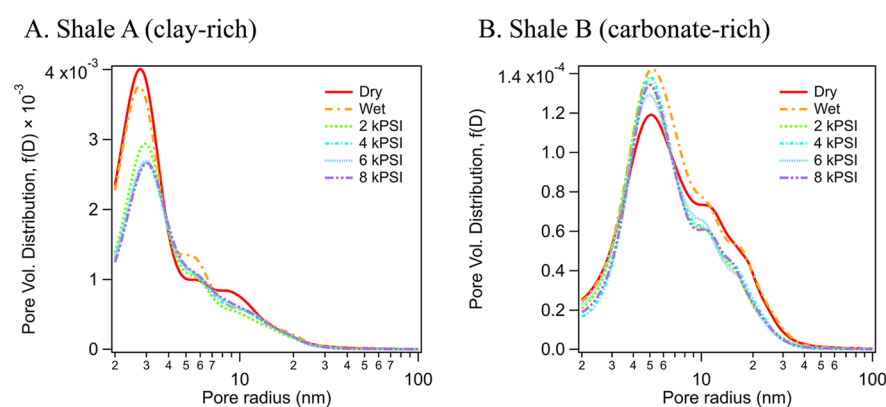


**Figure 2.** Volume-weighted pore size distributions for (A) clay-rich shale and (B) carbonate-rich shale calculated using Irena software.

Our analysis of the pore size distributions and fluid accessibility requires that we have estimates of the power law scatter typically observed in geomaterials such as shale. To treat the anisotropy of sample A, the 2D scattering profiles were sectioned and averaged at  $15^\circ$  increments along the major and minor axes of the scattering ellipse. This was repeated for both the 3 and 12 m sample-to-detector distances for every pressure condition. In each case, the low  $Q$  region shows a power law with an exponent that does not change significantly between the major and minor elliptical axes (Figures S6 and S7). This result allows us to simplify the data analysis using the radially averaged intensity.<sup>40</sup>

Figures 1A and 1B show the SANS plots,  $I(Q)$  vs  $Q$  for Shale A and B samples, respectively. Qualitatively, there are clear differences between the two shale samples. In particular, the shape of the Shale A scattering curve changes as pressure increases, developing a bend at  $Q \approx 0.02 \text{ \AA}^{-1}$  where intensity decreases more significantly with increasing pressure at lower  $Q$  (inset in Figure 1A). For Shale B, on the other hand, the scattering curve retained approximately the same scattering power law with pressure over the observed  $Q$ -domain. For both shale samples, decreases in intensity at higher pressures result, at least in part, from the pressure dependence of pore accessibility to the contrast matching fluid.

**3.3. Pore Size Distribution and Accessibility.** The fitting tool in Irena was used to calculate the PDF (eq 2) after factoring out the low  $Q$  power law scatter. In the case of carbonate-rich shale (Shale B), where the fitted power law exponent is approximately 4, it is a safe assumption, as this

value for the exponent indicates that scatter is caused by large pore surface features outside of the region of interest, where there is no information on the size distribution function. For the clay-rich shale, however, the power law exponent being between 3 and 4 introduces uncertainty in terms of whether this scattering is due to polydispersity or surface structure. The low  $Q$  limits of the SANS measurement does not give sufficient information on the larger length scale structures to resolve this question.

Figure 2 plots the volume-weighted pore size distributions for the two shale samples. Fitted SANS profiles and power law exponents for representative pressures can be found in Figure S8. Porod exponents ranged from 3.63 for the dry Shale A sample to 3.32 for Shale A at 8 kPSI and from 4.22 for the dry Shale B sample to 4.01 for Shale B at 8 kPSI. Parameters, including the minimum and maximum diameters, were varied to ensure that the fitted distribution curves did not change significantly.

The assumption that low  $Q$  scattering is due to surface structure will have the biggest impact on the distribution of larger pores. Using the fitting software, the power law exponent value for the clay-rich shale was varied between 3 and 4, and although there were changes in the absolute  $f(D)$  value, the relative pore sizes in the fitting region of interest ( $\sim 2$  to 50 nm radius pores) did not change. Observed trends therefore apply only to the relative changes in this region and should not be taken as a complete size distribution of pores up to 100 nm in radius.

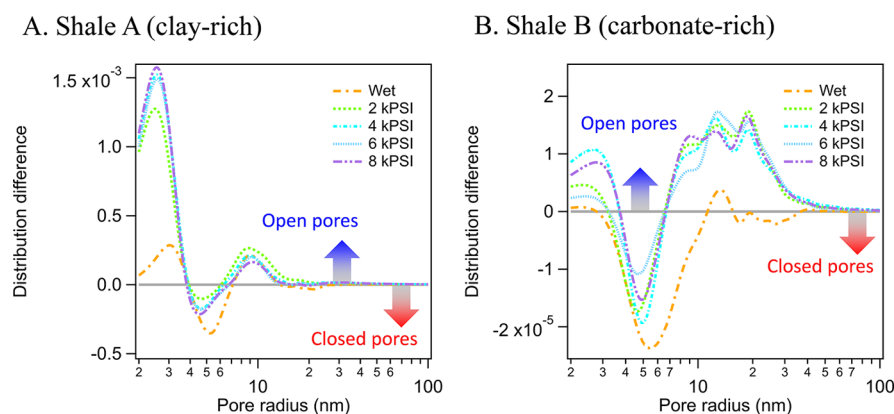


**Figure 3.** Differences in the pore size distributions for (A) clay-rich shale and (B) carbonate-rich shale show regions of pore accessibility to water, as well as regions where pores are closed off to water even at elevated pressures.

For Shale A (Figure 2A), significant differences in the size distribution are observed with increasing pressure. Pores with a radius of 2–3 nm were the dominant size and their relative abundance decreased when contrast matching  $\text{H}_2\text{O}/\text{D}_2\text{O}$  was added, indicating that these pores are accessible to water even without added pressure. Saturation testing also shows a consistent trend with Shale A results, in that initial exposure to water immediately filled the smallest sized pores. When pressure was increased to 2 kPSI (13.8 MPa) and again to 4 kPSI (27.6 MPa), this peak dropped further. There was an additional, smaller population of pores with a radius around 10 nm, which showed a similar decrease when water was added. In between, there is a region with a pore size around 5 nm which increased in abundance after water was introduced to the system, indicating that these pores are closed to the contrast matching fluid.

Carbonate-rich Shale B presented a different trend in pore size distribution (Figure 2B). For the dry shale, the average pore size was significantly larger, with few 2–3 nm pores. This is expected due to its low contents of clay and organic matter, which typically host smaller pores.<sup>42,43</sup> As pressure increased, similarly to Shale A, there was a region with a pore radius around 5 nm which had increasing abundance, while larger pores decreased in abundance, indicating accessibility to the contrast matching fluid. There did not appear to be significant changes in abundance after reaching a pressure of 2 kPSI, indicating all accessible porosity may be filled at this point.

To better visualize these relative changes, the pore size distribution of the wet and higher pressure samples were subtracted from the dry pore size distribution (Figure 3). When the distribution is higher than that of the dry shale sample, the negative sign of this difference indicates that pores are less accessible to water. When the distribution is lower, i.e., there are less of these sized pores in the wetted/pressurized samples, the positive sign indicates that these pores are more accessible to water.

For both the carbonate-rich and clay-rich shales, there was a pore radius region between 4 and 10 nm where pores were closed off to water in the system without any additional pressure. When pressure was increased to 2 kPSI (13.8 MPa), some of the larger pores in this region became accessible; however, a population of pores with an average radius of around 5 nm remained closed to water even at the highest pressure of 8 kPSI (55.1 MPa). In the clay-rich Shale A, there was a large peak in accessible pores with a radius between 2

and 3 nm. These pores reached their peak in accessibility after increasing pressure to 4 kPSI (27.6 MPa) and accounted for a majority of the measured porosity in the sample. Shale B also had a population of these 2–3 nm pores, but it was much smaller. The majority of open pores in the carbonate-rich shale were larger than 6 nm in radius, and the distribution difference did not change significantly after reaching 2 kPSI, indicating that the maximum accessibility occurs at a lower pressure.

Changes in the accessibility of these pores is likely related to their location within the shale matrix. Porosity in shale consists of organic matter porosity, intraparticle porosity, and interparticle porosity.<sup>44</sup> This porosity is generally classified into micropores, mesopores, and macropores, which have pore sizes of <2 nm, 2–50 nm, and >50 nm, respectively. Previous studies have found that the smallest shale pores correspond with high clay mineral content. For example, Saidian et al.<sup>43</sup> studied shales with varying compositions from the Haynesville, Niobrara, Monterey, and Eastern European Silurian Formations and found that shales with a high clay content and a low organic matter content had more porosity in the small mesopore range (<10 nm), while shales with a low clay content and a high organic matter content had more porosity in the larger mesoporous (10–50 nm) and macroporous ranges. However, these studies provided only limited quantification of micropores, as the mercury intrusion porosimetry technique cannot measure pores with a throat diameter less than 3.6 nm. A separate study by Kuila et al.<sup>42</sup> used gas adsorption to study the pore size distribution of shales with increasing clay content. It was found that as the clay content increased, 2–3 nm pores became more abundant. The greater abundance was attributed to an increase in intratactoid clay pore space, which hosts pores in this size range.

Thus, the less accessible pore size region in our shales is presumed to consist primarily of organic porosity, while the smaller accessible pores are in clay. This is consistent with wettability trends, as organic matter is expected to be more hydrophobic than clay minerals. Although the carbonate-rich shale did not have detectable organic content and only had a small percentage of clay minerals, small quantities of this porosity type are expected to be overrepresented in nanopore characterization, as they host the majority of small pores. Furthermore, the magnitude of the open and closed porosity in this region is much higher for the clay-rich shale, which is consistent with QXRD and TG/DSC observations.

**3.4. Porosity and Closed Pore Percentages.** The pore size distribution calculation provides insight into the discrimination of differently sized pores toward being filled by the contrast matching water solution at elevated pressures. However, it is also useful to quantify the overall characteristics of the shale. Therefore, we calculated porosity and the percentage of closed pores over the measured  $Q$  range using SANS data.

A more complete analysis of the porosity,  $\phi$ , from the available data was calculated using the Porod invariant,  $Z$ :<sup>38</sup>

$$Z = \int_0^{\infty} Q^2 I(Q) dQ = 2\pi^2 (\Delta\rho^*)^2 \phi (1 - \phi) \quad (5)$$

where  $\Delta\rho^*$  is the scattering length density contrast. Clarkson et al.<sup>45</sup> showed small differences of about 0.5% in porosity when extrapolating to cover the  $Q$  range of 0 to infinity rather than using the measured  $Q$  range. We instead limited the calculation to the measured SANS region. This form of the invariant is based on the assumption that the power law segment of the SANS is due to polydisperse spheroids. We use this form as our view of the voids is from the direction where the SANS is approximately isotropic; thus we have insufficient information on the anisotropy to use the form which takes this feature into account.<sup>40,41</sup> This may result in an underestimation of the total porosity.

The calculated accessible porosity and closed pore fractions for the two shales can be found in Figure 4. The dashed line indicates the porosity calculated for the “dry” sample, e.g., the air-filled porosity. The first data point at ambient pressure is the “wet” sample porosity, e.g., the contrast fluid-filled porosity. With additional pressure, previously inaccessible

pores became accessible to the contrast matching solution. This change was used to calculate increases in the water-filled porosity, as shown on the figures. The difference between this porosity and the dry porosity (e.g., total porosity) was used to calculate the fraction of closed pores.

Shale A had a much higher air-filled porosity of 7.7% compared with the Shale B air-filled porosity of 0.51%. However, with increased pressure, Shale A showed a higher fraction of closed pores than Shale B, i.e., 0.078 compared with 0.026 at 8 kPSI. This is consistent with pore size distribution observations showing closed pores in Shale A.

When taken in conjunction with the other analyses performed in this study, porosity results provide further insight into how the pore network varies between the two mineralogically distinct shale samples. Comparison of the size-dependent pore accessibility, shown in Figure 3, indicates that the more tortuous pore network of clay-rich shales requires increased pressure to maximize pore accessibility and further establishes the existence of a distinct pore size range within the shale that is not accessible to water, even at elevated pressures. This size range, which is more abundant in the clay-rich shale, likely contributes to the higher closed porosity in the clay-rich sample. Relative to clay-rich shale, carbonate-rich shale has a lower percentage of closed pores. However, it also has a lower porosity and is likely less hydrocarbon-rich due to its low kerogen content. Although the closed porosity is a small percentage of total porosity, these pores fall primarily in a size range indicating that they are hosted by organic matter. It is well documented that organic nanopores are the main storage space for shale gas.<sup>46–48</sup> Thus, it is very important to understand water interactions with these pores at high pressure to maximize recovery.

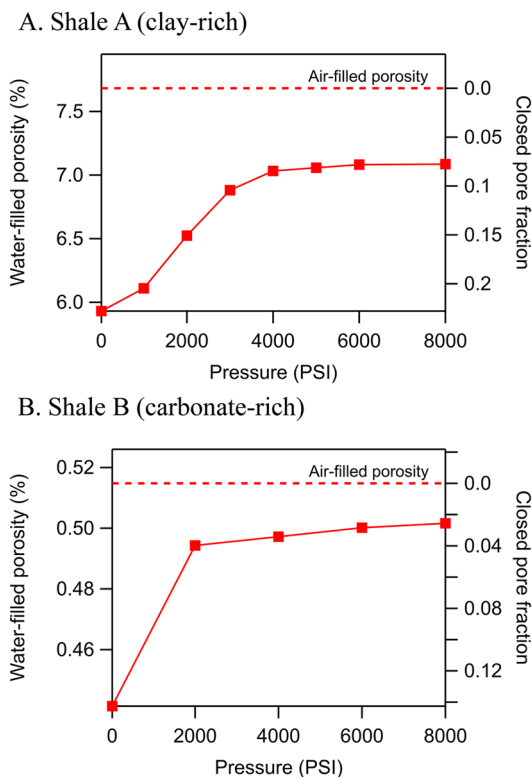


**Figure 4.** Water-filled porosity and closed pore fractions for (A) clay-rich shale and (B) carbonate-rich shale under increasing compressive and hydrostatic fluid pressures.

## 4. CONCLUSIONS

SANS analysis provides many new insights into the characteristics of clay- and carbonate-rich shales and can help us to estimate their responses to the elevated pressures introduced during hydraulic fracturing operations. For example, while the clay-rich shale had a much higher porosity than the carbonate-rich shale, a larger percentage of these pores remained closed to water even at an elevated pressure of 8 kPSI (55.1 MPa). By characterizing the pore accessibility and pore size distribution, we have shown that these closed pores have a radii around 5 nm. Furthermore, accessible pores existed that were both larger and smaller than the closed pore sizes, indicating that these pores may be closed to water due to the hydrophobic nature of the pore host material, i.e., organic matter. The behavior of these nanopores under pressure is an important consideration because pressure management is one of the few tools that well operators can use to improve recovery and minimize operational costs after well establishment. Thus, our finding that the closed pore fraction is essentially minimized after 2000 PSI for carbonate-rich shale and 4000 PSI for clay-rich shale can be incorporated into well operation to minimize costs associated with higher-than-necessary pressurization.

Clay- and carbonate-rich shales can coexist, often in close proximity, in unconventional shale formations. It is therefore vital to consider the variations in nanoporosity and pore accessibility to conduct effective hydraulic fracturing operations. For example, the closed pores likely correspond with kerogen-rich pores that store hydrocarbons. In addition, due to the more tortuous pore network in clay-rich shales, flow from these pores may be decreased or the resource confined entirely,

leading to lower recovery. These new quantitative and qualitative insights can also be used to advance models of novel enhanced oil recovery strategies and improve our understanding of why some formations struggle with low recoveries and rapid production decline while others perform better than expected.

## ■ ASSOCIATED CONTENT

### SI Supporting Information

The Supporting Information is available free of charge at <https://pubs.acs.org/doi/10.1021/acs.energyfuels.0c01009>.

Additional figures showing duplicate measurements, anisotropy analysis, and fitted scattering profiles (PDF)

## ■ AUTHOR INFORMATION

### Corresponding Author

Chelsea W. Neil – *Earth and Environmental Sciences Division, Los Alamos National Laboratory, Los Alamos, New Mexico 87545, United States*; [orcid.org/0000-0002-7679-157X](https://orcid.org/0000-0002-7679-157X); Phone: (908)-489-4463; Email: [cwneil@lanl.gov](mailto:cwneil@lanl.gov)

### Authors

Rex P. Hjelm – *Materials Science and Technology Division, Los Alamos National Laboratory, Los Alamos, New Mexico 87545, United States*

■ Marilyn E. Hawley – *Materials Science and Technology Division, Los Alamos National Laboratory, Los Alamos, New Mexico 87545, United States*

Erik B. Watkins – *Materials Physics and Applications Division, Los Alamos National Laboratory, Los Alamos, New Mexico 87545, United States*; [orcid.org/0000-0001-8573-9629](https://orcid.org/0000-0001-8573-9629)

Cody Cockreham – *Earth and Environmental Sciences Division, Los Alamos National Laboratory, Los Alamos, New Mexico 87545, United States; Voiland School of Chemical Engineering and Bioengineering and Alexandra Navrotsky Institute for Experimental Thermodynamics, Washington State University, Pullman, Washington 99164, United States*

Di Wu – *Voiland School of Chemical Engineering and Bioengineering, Alexandra Navrotsky Institute for Experimental Thermodynamics, Materials Science and Engineering, and Department of Chemistry, Washington State University, Pullman, Washington 99164, United States*; [orcid.org/0000-0001-6879-321X](https://orcid.org/0000-0001-6879-321X)

Yimin Mao – *NIST Center for Neutron Research, National Institute of Standards and Technology, Gaithersburg, Maryland 20899, United States*; [orcid.org/0000-0002-6240-3791](https://orcid.org/0000-0002-6240-3791)

Timothy B. Fischer – *Chevron Energy Technology Company, Houston, Texas 77042, United States*

M. Rebecca Stokes – *Chevron Energy Technology Company, Houston, Texas 77042, United States*

Hongwu Xu – *Earth and Environmental Sciences Division, Los Alamos National Laboratory, Los Alamos, New Mexico 87545, United States*

Complete contact information is available at: <https://pubs.acs.org/doi/10.1021/acs.energyfuels.0c01009>

### Author Contributions

C.W.N. contributed to conducting the SANS experiments and SAN data analysis and took the lead in writing the manuscript. R.P.H. provided SANS theory and, with M.E.H. and E.B.W., conducted SANS measurements. C.C. and D.W. conducted TGA/DSC analysis. Y.M. supervised the SANS experiments.

T.B.F., M.R.S., and H.X. conceived the study, acquired funding, and supervised the project. All authors provided substantial input to the final manuscript.

### Notes

The authors declare no competing financial interest.  
■ M.E.H. is currently retired.

## ■ ACKNOWLEDGMENTS

This work was supported by the Chevron Energy Technology Company through a CRADA to the Los Alamos National Laboratory (LANL) (Project PIs: M. Rebecca Stokes and Hongwu Xu). LANL is operated by Triad National Security, LLC, for the National Nuclear Security Administration of the U.S. Department of Energy (contract no. 89233218NCA000001). Access to small angle neutron scattering instrumentation was provided by the Center for High Resolution Neutron Scattering, a partnership between the National Institute of Standards and Technology and the National Science Foundation under agreement no. DMR-1508249. Di Wu acknowledges the institutional funds from the Gene and Linda Voiland School of Chemical Engineering and Bioengineering and the fund of Alexandra Navrotsky Institute for Experimental Thermodynamics at Washington State University.

## ■ REFERENCES

- (1) U.S. Energy Information Administration. *Annual Energy Outlook 2019: With Projections to 2050*; Government Printing Office: 2019.
- (2) Paltsev, S.; Jacoby, H. D.; Reilly, J. M.; Ejaz, Q. J.; Morris, J.; O'Sullivan, F.; Rausch, S.; Winchester, N.; Kragha, O. The future of US natural gas production, use, and trade. *Energy Policy* **2011**, *39* (9), 5309–5321.
- (3) Kilian, L. The impact of the shale oil revolution on US oil and gasoline prices. *Review of Environmental Economics and Policy* **2016**, *10* (2), 185–205.
- (4) Hubbert, M. K.; Willis, D. G. Mechanics of hydraulics fracturing. *Trans. Soc. Pet. Eng.* **1957**, *210*, 153–163.
- (5) Crittendon, B. C. The mechanics of design and interpretation of hydraulic fracture treatments. *JPT, J. Pet. Technol.* **1959**, *11* (10), 21–29.
- (6) Zhang, X.; Lu, Y.; Tang, J.; Zhou, Z.; Liao, Y. Experimental study on fracture initiation and propagation in shale using supercritical carbon dioxide fracturing. *Fuel* **2017**, *190*, 370–378.
- (7) Zang, A.; Stephansson, O.; Stenberg, L.; Plenkers, K.; Specht, S.; Milkereit, C.; Schill, E.; Kwiatek, G.; Dresen, G.; Zimmermann, G.; Dahm, T.; Weber, M. Hydraulic fracture monitoring in hard rock at 410 m depth with an advanced fluid-injection protocol and extensive sensor array. *Geophys. J. Int.* **2017**, *208* (2), 790–813.
- (8) Wang, S. Y.; Sun, L.; Au, A. S. K.; Yang, T. H.; Tang, C. A. 2D-numerical analysis of hydraulic fracturing in heterogeneous geomaterials. *Construction and Building Materials* **2009**, *23* (6), 2196–2206.
- (9) Ruppert, L. F.; Sakurovs, R.; Blach, T. P.; He, L.; Melnichenko, Y. B.; Mildner, D. F.; Alcantar-Lopez, L. A USANS/SANS study of the accessibility of pores in the Barnett Shale to methane and water. *Energy Fuels* **2013**, *27* (2), 772–779.
- (10) Melnichenko, Y. B.; He, L.; Sakurovs, R.; Kholodenko, A. L.; Blach, T.; Mastalerz, M.; Radliński, A. P.; Cheng, G.; Mildner, D. F. Accessibility of pores in coal to methane and carbon dioxide. *Fuel* **2012**, *91* (1), 200–208.
- (11) Bahadur, J.; Melnichenko, Y. B.; He, L.; Contescu, C. I.; Gallego, N. C.; Carmichael, J. R. SANS investigations of CO<sub>2</sub> adsorption in microporous carbon. *Carbon* **2015**, *95*, 535–544.
- (12) Zhang, R.; Liu, S.; Bahadur, J.; Elsworth, D.; Melnichenko, Y.; He, L.; Wang, Y. Estimation and modeling of coal pore accessibility using small angle neutron scattering. *Fuel* **2015**, *161*, 323–332.

- (13) Xu, H. Probing nanopore structure and confined fluid behavior in shale matrix: A review on small-angle neutron scattering studies. *Int. J. Coal Geol.* **2020**, *217*, 103325.
- (14) Mang, J. T.; Skidmore, C. B.; Hjelm, R. P.; Howe, P. M. Application of small-angle neutron scattering to the study of porosity in energetic materials. *J. Mater. Res.* **2000**, *15* (5), 1199–1208.
- (15) Hjelm, R. P.; Taylor, M. A.; Frash, L. P.; Hawley, M. E.; Ding, M.; Xu, H.; Barker, J.; Olds, D.; Heath, J.; Dewers, T. Flow-through compression cell for small-angle and ultra-small-angle neutron scattering measurements. *Rev. Sci. Instrum.* **2018**, *89* (5), 055115.
- (16) Xu, H.; Zhao, Y.; Zhang, J.; Hickmott, D. D.; Daemen, L. L. In situ neutron diffraction study of deuterated portlandite  $\text{Ca}(\text{OD})_2$  at high pressure and temperature. *Phys. Chem. Miner.* **2007**, *34* (4), 223–232.
- (17) Zhao, Y.; Xu, H.; Daemen, L. L.; Lokshin, K.; Tait, K. T.; Mao, W. L.; Luo, J.; Currier, R. P.; Hickmott, D. D. High-pressure/low-temperature neutron scattering of gas inclusion compounds: Progress and prospects. *Proc. Natl. Acad. Sci. U. S. A.* **2007**, *104* (14), 5727–5731.
- (18) Clarkson, C. R.; Solano, N.; Bustin, R. M.; Bustin, A. M. M.; Chalmers, G. R. L.; He, L.; Melnichenko, Y. B.; Radliński, A. P.; Blach, T. P. Pore structure characterization of North American shale gas reservoirs using USANS/SANS, gas adsorption, and mercury intrusion. *Fuel* **2013**, *103*, 606–616.
- (19) Gu, X.; Mildner, D. F. R. Ultra-small-angle neutron scattering with azimuthal asymmetry. *J. Appl. Crystallogr.* **2016**, *49* (3), 934–943.
- (20) King, H. E., Jr; Eberle, A. P.; Walters, C. C.; Klier, C. E.; Ertas, D.; Huynh, C. Pore architecture and connectivity in gas shale. *Energy Fuels* **2015**, *29* (3), 1375–1390.
- (21) Mastalerz, M.; He, L.; Melnichenko, Y. B.; Rupp, J. A. Porosity of coal and shale: Insights from gas adsorption and SANS/USANS techniques. *Energy Fuels* **2012**, *26* (8), 5109–5120.
- (22) Środoń, J.; Driess, V. A.; McCarty, D. K.; Hsieh, J. C.; Eberl, D. D. Quantitative X-Ray diffraction analysis of clay-bearing rocks from random preparations. *Clays Clay Miner.* **2001**, *49* (6), 514–528.
- (23) Omotoso, O.; McCarty, D. K.; Hillier, S.; Kleeberg, R. Some successful approaches to quantitative mineral analysis as revealed by the 3rd Reynolds Cup contest. *Clays Clay Miner.* **2006**, *54* (6), 748–760.
- (24) Chung, F. H. Quantitative interpretation of X-ray diffraction patterns of mixtures. I. Matrix-flushing method for quantitative multicomponent analysis. *J. Appl. Crystallogr.* **1974**, *7* (6), 519–525.
- (25) Okiongbo, K. S.; Aplin, A. C.; Larter, S. R. Changes in type II kerogen density as a function of maturity: Evidence from the Kimmeridge Clay Formation. *Energy Fuels* **2005**, *19* (6), 2495–2499.
- (26) Jarvie, D. M. Chapter 11: Total organic carbon (TOC) analysis. In *Treatise of Petroleum Geology: Handbook of Petroleum Geology, Source and Migration Processes, and Education Techniques*; Merrill, R., Ed.; American Association of Petroleum Geologists: Tulsa, Oklahoma, 1991; pp 113–118.
- (27) Guo, X.; Xu, H. Enthalpies of formation of polyhalite: A mineral relevant to salt repository. *J. Chem. Thermodyn.* **2017**, *114*, 44–47.
- (28) Xu, H.; Navrotsky, A.; Nyman, M. D.; Nenoff, T. M. Thermochemistry of microporous silicotitanate phases in the  $\text{Na}_2\text{O}-\text{Cs}_2\text{O}-\text{SiO}_2-\text{TiO}_2-\text{H}_2\text{O}$  system. *J. Mater. Res.* **2000**, *15* (3), 815–823.
- (29) Xu, H.; Zhang, Y.; Navrotsky, A. Enthalpies of formation of microporous titanosilicates ETS-4 and ETS-10. *Microporous Mesoporous Mater.* **2001**, *47* (2–3), 285–291.
- (30) Hirono, T.; Sakaguchi, M.; Otsuki, K.; Sone, H.; Fujimoto, K.; Mishima, T.; Lin, W.; Tanikawa, W.; Tanimizu, M.; Soh, W.; Yeh, E. C.; Song, S.-R. Characterization of slip zone associated with the 1999 Taiwan Chi-Chi earthquake: X-ray CT image analyses and microstructural observations of the Taiwan Chelungpu fault. *Tectonophysics* **2008**, *449* (1–4), 63–84.
- (31) Xu, H.; Zhao, Y.; Vogel, S. C.; Daemen, L. L.; Hickmott, D. D. Anisotropic thermal expansion and hydrogen bonding behavior of portlandite: A high-temperature neutron diffraction study. *J. Solid State Chem.* **2007**, *180* (4), 1519–1525.
- (32) Xu, H.; Zhao, Y.; Hickmott, D. D.; Lane, N. J.; Vogel, S. C.; Zhang, J.; Daemen, L. L. High-temperature neutron diffraction study of deuterated brucite. *Phys. Chem. Miner.* **2013**, *40* (10), 799–810.
- (33) Schaefer, D. W.; Rieker, T.; Agamalian, M.; Lin, J. S.; Fischer, D.; Sukumaran, S.; Chen, C.; Beaucage, G.; Herd, C.; Ivie, J. Multilevel structure of reinforcing silica and carbon. *J. Appl. Crystallogr.* **2000**, *33* (3), 587–591.
- (34) Fratzl, P. Small-angle scattering in materials science—a short review of applications in alloys, ceramics and composite materials. *J. Appl. Crystallogr.* **2003**, *36* (3), 397–404.
- (35) Glinka, C. J.; Barker, J. G.; Hammouda, B.; Krueger, S.; Moyer, J. J.; Orts, W. J. The 30 m small-angle neutron scattering instruments at the National Institute of Standards and Technology. *J. Appl. Crystallogr.* **1998**, *31* (3), 430–445.
- (36) Kline, S. R. Reduction and analysis of SANS and USANS data using IGOR Pro. *J. Appl. Crystallogr.* **2006**, *39* (6), 895–900.
- (37) Ilavsky, J.; Jemian, P. R. Irena and Indra SAXS data analysis macros, including maximum entropy. Argonne National Laboratory: 2008. <https://usaxs.xray.aps.anl.gov/software/irena> (accessed 2020-06-29).
- (38) Porod, G. General Theory. In *Small Angle X-ray Scattering*; Glatter, O., Kratky, O., Eds.; Academic Press: London, 1982; pp 17–51.
- (39) Sun, M.; Yu, B.; Hu, Q.; Yang, R.; Zhang, Y.; Li, B.; Melnichenko, Y. B.; Cheng, G. Pore structure characterization of organic-rich Niutitang shale from China: Small angle neutron scattering (SANS) study. *Int. J. Coal Geol.* **2018**, *186*, 115–125.
- (40) Gu, X.; Cole, D. R.; Rother, G.; Mildner, D. F.; Brantley, S. L. Pores in Marcellus shale: a neutron scattering and FIB-SEM study. *Energy Fuels* **2015**, *29* (3), 1295–1308.
- (41) Gu, X.; Mildner, D. F.; Cole, D. R.; Rother, G.; Slingerland, R.; Brantley, S. L. Quantification of organic porosity and water accessibility in Marcellus shale using neutron scattering. *Energy Fuels* **2016**, *30* (6), 4438–4449.
- (42) Kuila, U. Measurement and interpretation of porosity and pore-size distribution in mudrocks: The hole story of shales. Doctoral dissertation, Colorado School of Mines, 2011.
- (43) Saidian, M.; Kuila, U.; Prasad, M.; Barraza, S. R.; Godinez, L. J.; Alcantar-Lopez, L. A comparison of measurement techniques for porosity and pore size distribution in mudrocks: a case study of Haynesville, Niobrara, Monterey and Eastern European Silurian Formations. *AAPG Memoir* **2016**, *110*, 89–144.
- (44) Loucks, R. G.; Ruppel, S.; Reed, R. M.; Hammes, U.; Zahm, C. Origin and classification of pores in mudstones from shale-gas systems. In *Proceedings of the 2011 AAPG International Conference and Exhibition*, Milan, Italy, October 3–26, 2011; Datapages, Inc. Search and Discovery: 2011; pp 1–32.
- (45) Clarkson, C. R.; Freeman, M.; He, L.; Agamalian, M.; Melnichenko, Y. B.; Mastalerz, M.; Bustin, R. M.; Radliński, A. P.; Blach, T. P. Characterization of tight gas reservoir pore structure using USANS/SANS and gas adsorption analysis. *Fuel* **2012**, *95*, 371–385.
- (46) Borjigin, T.; Shen, B.; Yu, L.; Yang, Y.; Zhang, W.; Tao, C.; Xi, B.; Zhang, Q.; Bao, F.; Qin, J. Mechanisms of shale gas generation and accumulation in the Ordovician Wufeng-Longmaxi Formation, Sichuan Basin, SW China. *Petroleum Exploration and Development* **2017**, *44* (1), 69–78.
- (47) Liang, F.; Bai, W.; Zou, C.; Wang, H.; Wu, J.; Ma, C.; Zhang, Q.; Guo, W.; Sun, S.; Zhu, Y.; Cui, H.; Liu, D. Shale gas enrichment pattern and exploration significance of Well WuXi-2 in northeast Chongqing, NE Sichuan Basin. *Petroleum Exploration and Development* **2016**, *43* (3), 386–394.
- (48) Wang, P.; Jiang, Z.; Han, B.; Lv, P.; Jin, C.; Zhang, K.; Li, X.; Li, T. Reservoir characteristics and controlling factor of shale gas in Lower Cambrian Niutitang Formation, South China. *Petroleum Research* **2018**, *3* (3), 210–220.